PAPER

Check for updates

Synthesis of self-assembled mesoporous 3D In_2O_3 hierarchical micro flowers composed of nanosheets and their electrochemical properties†

Balasubramaniam Arul Prakasam, [ID] *[ab] Manu Lahtinen, [ID] [c] Anssi Peuronen, [ID] [c] Govindhasamy Manikandan,[b] Manickavachagam Muruganandham[a] and Mika Sillanpää[ad]

This report describes the methodology for the fabrication of mesoporous In_2O_3 microflowers by hydrothermal and calcination procedures in which $In(OH)_3/In_2S_3$ acts as an intermediate. Both In_2O_3 and its precursor were analyzed with scanning electron microscopy, energy dispersive X-ray spectrophotometry, transmission electron microscopy and powder X-ray diffraction. BET surface area, pore size and pore volume analyses were also carried out. Electron microscopy images clearly evidence the self-assembly of 2D nanosheets into the micro flower structure. The mechanism of self-assembly and calcination is reported. Electrochemical properties of the synthesized In_2O_3 micro flowers were studied.

1. Introduction

The synthesis of semiconductor nanomaterials with extraordinary shapes and structures are of great interest since these properties can significantly influence the semiconducting properties of such materials. Therefore, the development of synthetic pathways that give rise to certain nanoscopic features is important. Decomposition of simple precursor components in benign hydrothermal conditions presents an interesting strategy to yield novel nanosized 3D structures with a large surface area. One semiconducting material, which represents a suitable candidate for such an approach, is indium(III) oxide, In_2O_3, which has a wide band gap of 3.55–3.75 eV (analogous to GaN). In_2O_3 has been shown to have many promising utilization areas such as gas sensors, solar cells and flat-panel displays.[1–6] Versatile morphological properties of In_2O_3 are demonstrated in several studies, wherein various shapes, such as nanocubes, nanorods and microspheres, have been reported.[7–23] Generally, $In(OH)_3$ and InOOH are used as precursors for the synthesis of In_2O_3.[7–20] Synthesis of In_2O_3 via $In(OH)_3/In_2S_3$ as an intermediate mesostructure, followed by calcination, presents an

interesting option which allows variation of morphology and porosity due to the intermediate structure which is eventually oxidized to In_2O_3.[21–33] There are some latest reports on the fabrication and characterization of morphologically interesting nano materials.[34–37] Variation of the nanostructure using this synthetic pathway arises largely from the selection of the precursor components. Although many organic compounds can be used as a sulfur source, careful selection is obligatory as the organic compounds (if the process is free from calcination) can be incorporated with the positively charged metal ions on the surface of nanoparticles and thereby limit the mobility of the charge carrier in electronic devices. Dithiobiuret is an interesting candidate in this regard as the decomposition products are volatile and hence the formed nanoparticles will be free from organic impurities.

One of our particular areas of interest is morphosynthesis of porous hierarchical structures such as 3D microflowers.[38] Within this scope, we herein demonstrate the self-assembly of 3D structural template consisting of indium sulfide and hydroxide synthesized in hydrothermal conditions using dithiobiuret as the sulfur source and its subsequent calcination to a In_2O_3 nanostructure. The 3D In_2O_3 microflowers are formed by the aggregation of 2D nanoflakes with a high degree of compositional control. The structural and physical properties of these complex hierarchical structures are analyzed with SEM, EDX and TEM as well as by nitrogen adsorption analysis. Furthermore, the phase identification of samples was confirmed by powder X-ray diffraction (PXRD). An electrochemical study of the synthesized In_2O_3 micro flowers with an aim to understand the charge storage property has been carried out in detail.

[a]Department of Green Chemistry, School of Engineering Science, Lappeenranta University of Technology, Sammonkatu 12, FI-50130 Mikkeli, Finland. E-mail: arul7777@yahoo.com

[b]Department of Chemistry, Annamalai University, Annamalainagar, 608002, India

[c]Department of Chemistry, Laboratories of Inorganic and Analytical Chemistry, University of Jyväskylä, P. O. Box 35, FI-40014, Finland

[d]Department of Civil and Environmental Engineering, Florida International University, Miami, FL-33174, USA

† Electronic supplementary information (ESI) available. See DOI: 10.1039/c8ra03573c

2. Experimental details

2.1. Synthesis of indium oxide

Milli Q-Plus water (resistance = 18.2 M Ω) was used for all the experimental work. $In_2S_3/In(OH)_3$ micro flowers were prepared using indium nitrate (1.5 g, 5 mmol) and dithiobiuret (1.0 g, 7.5 mmol). Indium nitrate and dithiobiuret were separately dissolved in about 50 mL of water and heated till boiling. Hot solutions were mixed under stirring (200 rpm) and after 30 min the mixture was transferred into a 250 mL Teflon cup, which was further filled with 50 mL of water. Sealed Teflon vessel was put into a stainless steel shell and was autoclaved at 150 °C for 15 h. After the hydrothermal reaction, the flask was allowed to cool down to room temperature and the precipitate formed was filtered, washed with water and ethanol in order to eliminate possible impurities. It was then dried in an air oven at 120 °C for 2 h. In_2O_3 microflowers were prepared in hot air oven by calcinating the precursors ($In_2S_3/In(OH)_3$) at 600 °C for 6 h, followed by cooling down to room temperature before collecting the product. In this work, we aimed at the synthesis of structures with intriguing morphology, thus only the optimized reaction conditions are reported and the reaction conditions which resulted in inhomogeneous or broken morphologies are deliberately left out from the discussion.

2.2. SEM, TEM and powder PXRD measurements

The morphology of prepared bulk was examined using Hitachi S-4100 scanning electron microscope (SEM). Prior to SEM measurements, the samples were mounted on a carbon platform that was then coated with platinum using a magnetron sputter for 10 minutes. The ratio between In, S and O within the samples were analyzed using an energy-dispersive X-ray spectrophotometer installed in the scanning electron microscope. For transmission electron microscope (TEM) study, the sample was dispersed onto a Cu grid with holey carbon supporting films and studied at room temperature in a Tecnai F20 microscope operated at 200 kV. Powder X-ray diffraction (PXRD) was carried out using PANalytical X'Pert PRO diffractometer with Cu $K_{\alpha 1}$ radiation (1.5406 Å; 45 kV, 40 mA). A sample was placed on a silicon-made (producing zero-background signal) sample holder using petrolatum jelly as an adhesive. Data was recorded with X'Celerator detector in 2θ-range of 8–80° using step size of 0.02° and counting time of 140 s per step.

Average crystal sizes of the substances were determined using Scherrer equation (eqn (1)) and values were corrected by the instrumental broadening.

$$D = \frac{K\lambda}{\beta \cos\theta} \tag{1}$$

where in D stands for average size of the crystals, K as shape-dependent Scherrer's constant (0.9), λ as radiation wavelength (1.5406 Å), and β as integral breath given in radians subtracted by instrumental broadening (determined with a silicon standard measured using the above said experimental settings).

2.3. Electrochemical studies

Cyclic voltammetry studies were performed using SP-150, Bio-Logic Science Instruments. A three electrode cell configuration comprising active material coated glassy carbon electrode (area 0.071 cm^2), Pt wire and Ag/AgCl were used as the working, counter and reference electrodes respectively. For the fabrication of electrode, a mixture of 1 mg of active material (In_2O_3) and 1 ml of water was sonicated for 15 minutes and from the resultant suspension 5 microlitre was casted on GCE (working electrode).

3. Results and discussion

3.1. SEM analysis

The surface morphologies of the hydrothermal and calcinated products were further analyzed by SEM. From the SEM images of the hydrothermal product (Fig. 1) it was observed that the microstructures with flower-like morphology are formed with the size distribution of around 0.8 to 1.2 µm. Microflowers are built from small 2D nanosheets with thickness of 20–30 nm (Fig. 1e and f). These thin nanosheets, that are analogous to petals of flowers, are aligned to the spherical surface by pointing toward a common center. The microflower structures are highly dispersed and assembled by many interleaving and bending nanosheets with the thickness of less than 30 nm. From SEM or EDX we were unable to differentiate $In(OH)_3$ from In_2S_3 structures as the micro flowers exhibit peaks due to both oxygen and sulfur in EDX (Fig. S1†).

SEM images of the calcinated product (Fig. 2) showed that the morphology was conserved after calcination. However, thinning of nanosheet with curly structures, which are porous in nature, was observed. SEM image of In_2O_3 microflowers (Fig. 2) suggests that the petals with the sharp edges in the precursors are transformed into nanochain-like structures composed of small beads with the size of <10 nm (Fig. 2h). This is easily visualized by comparing the Fig. 1f and Fig. 2f–h. It is important to note that the overall dimensions of the micro-flowers stay intact during the calcination process; however, the formation of bead-like structures with the thinning of petals is evidenced. The petal thinning in microflowers as well as the deformation of sharp edges to bead-like structures are due to the removal of SO_2 from In_2S_3/In_3S_4 and H_2O from $In(OH)_3$ during calcination. Hence, the resulting In_2O_3 seems to exhibit porosity (Fig. 2f–h).

3.2. EDX analysis

EDX spectrum of the hydrothermal product (Fig. S1†) showed peaks arising from the presence of indium, sulfur and oxygen. The In, S and O atomic ratio was not in line with the general formula $In(OH)_3/In_2S_3$ as the hydrothermal product was a mixture of indium sulfides and indium oxide which is evident from the EDX analysis and was further confirmed from powder PXRD analysis (*vide infra*). The remaining peak observed at 1.5 keV is due to Al holder over which the sample was placed. EDX spectrum of calcinated product (Fig. S2†) is devoid of peak due to sulfur at 2.33 keV (KR1), which was intensely present in the
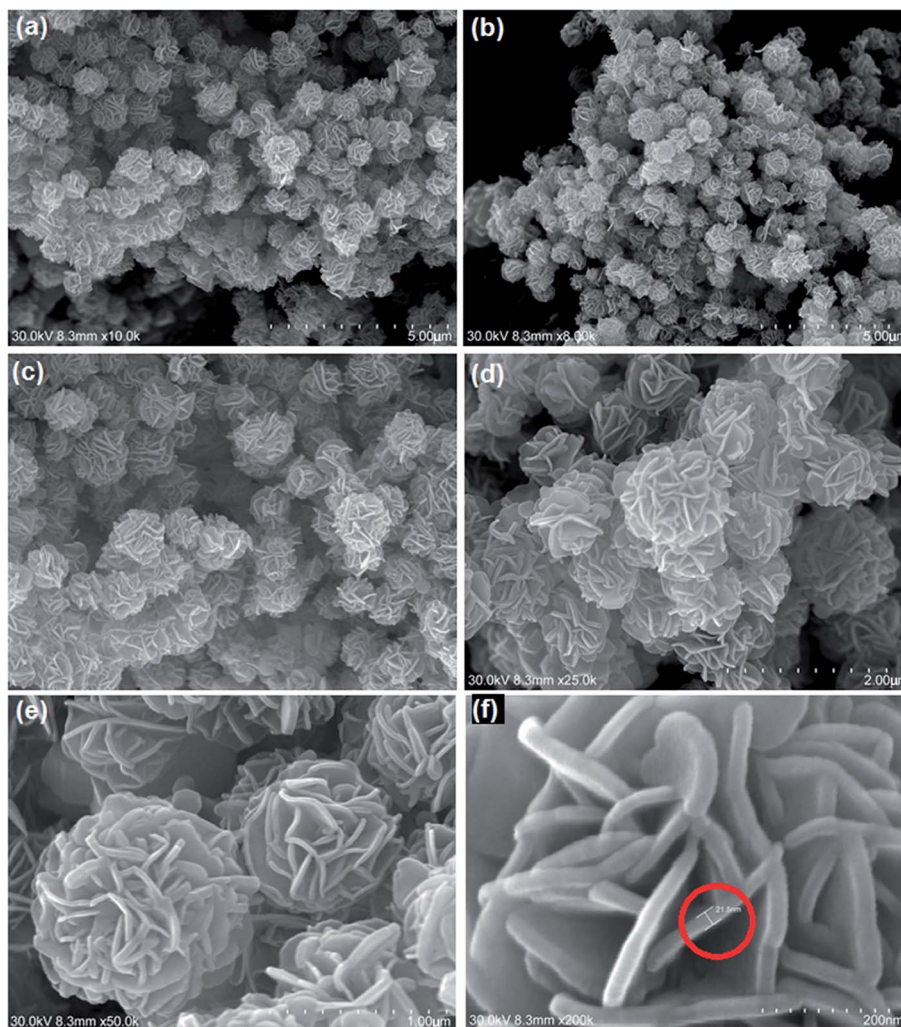
Fig. 1 SEM images of hydrothermal products; (a–d) mono-dispersed micro flower structures of hydrothermal products; (e) micro flowers composed of nano sheet (petals); (f) nano sheet with the breadth of 21.5 nm.

EDX of hydrothermal product. This shows the complete conversion of indium sulfides to indium oxide during calcination. The stoichiometry of indium and oxygen in the calcinated product was found to be closer to 2 : 3 indicating the formation of In_2O_3. This was further confirmed by PXRD analysis.

3.3. TEM analysis

TEM images of the hydrothermal products were shown in Fig. 3. The dark and light contrast (Fig. 3b, d, e and f) of the petals of the microflowers in TEM images are due to the difference in orientations of petals with respect to the electron beam. When the edges of the petals are parallel to electron beam it appears dark in contrast (Fig. 3d and e) whereas, when the surface of the petals is parallel to the electron beam they appear light in contrast (Fig. 3f). Similarly, the folded areas are also dark in contrast. TEM images of hydrothermal product clearly evidence the self-assembly of 2D nanosheets into microflower structure. The annular electron diffraction pattern indicates that the hydrothermal product is polycrystalline.

After calcination, retention of morphology (Fig. 4) and the thinning of petals or nanoflakes into wafer like structure were observed. In the calcinated product, the flakes are curved with wavy margins and the magnified view is shown in Fig. 4e and f, which reveals that the structure is highly porous as discussed above. It has been reported earlier[23] that the formation of porous structures in In_2O_3 is due to the distortion of crystal lattice by internal tensile stress as a result of change in bond parameters during the conversion of In_2S_3 to In_2O_3. The loss of H_2O and SO_2 molecules from the precursors ($In(OH)_3$ or In_2S_3 respectively) results in the formation of In_2O_3 nanoparticles with the size of 20 to 25 nm which are the basic building units of mesoporous hierarchical microflower structure. The TEM images Fig. 4e and f showed that the material is composed of particles.

3.4. X-ray diffraction analysis

The phase identification of samples was made by powder X-ray diffraction (PXRD). In the PXRD pattern of the hydrothermal product (Fig. S3†), characteristic diffraction peaks of In_2S_3, In_3S_4 and In_2O_3 phases can be identified indicating phase
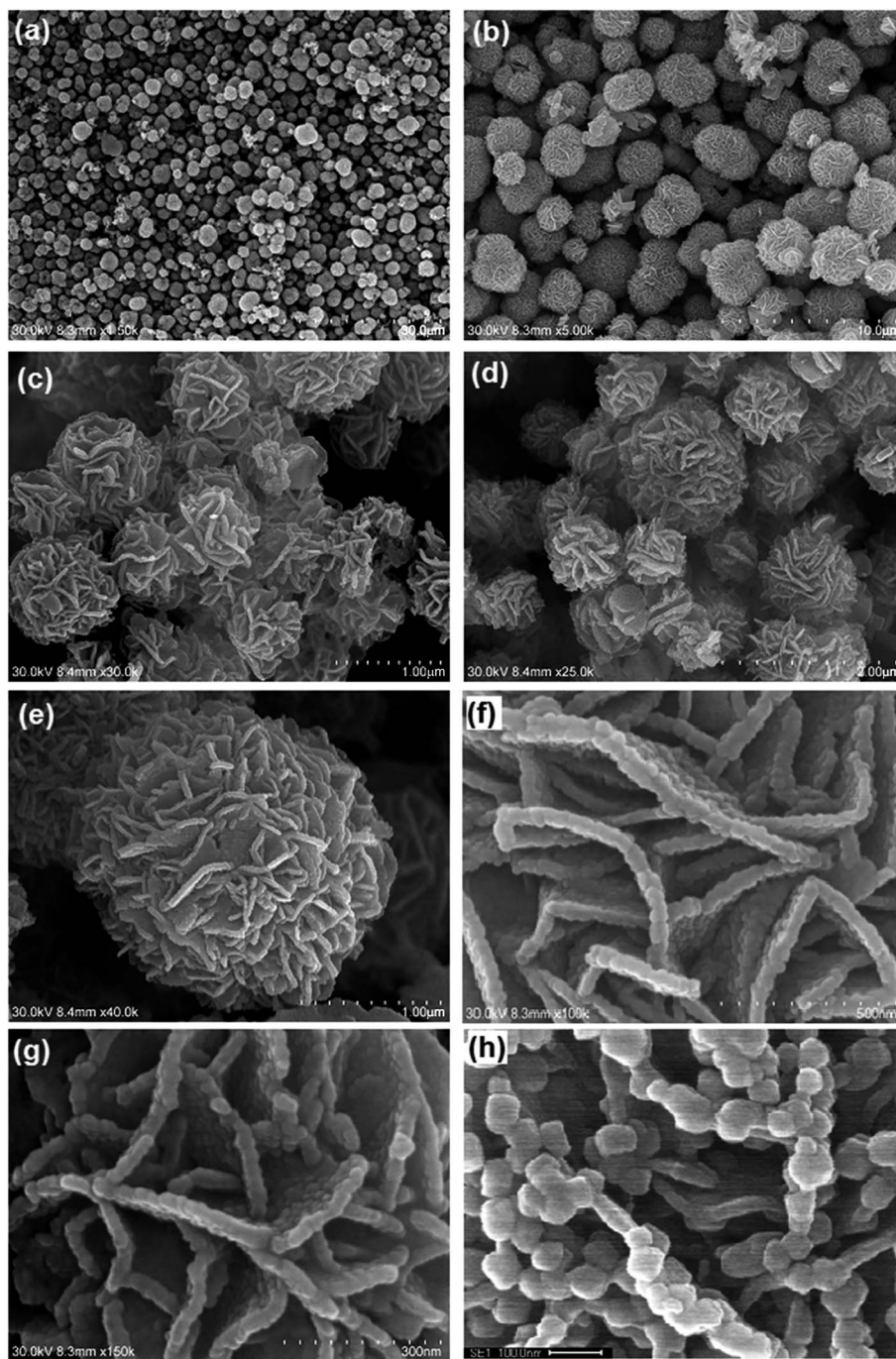
Fig. 2 SEM images of In_2O_3 microflowers; (a and b) homogeneous structure of microflowers; (c–e) microflowers with different dimensions (f and g) basic building units of microflowers (nanosheet) (h) bead-like structure in nanosheets.

mixture of all three. Similarly, after calcination at 400 °C for 2 h the PXRD pattern shows a mixture of In_3S_4 and In_2O_3 (Fig. S4†) indicating the conversion from In_2S_3 or In_3S_4 to In_2O_3 has occurred only partially. However, based on further calcination tests during which hydrothermal products were calcined at 600 °C for 6 h, In_2O_3 is the sole component as identified in the acquired PXRD pattern (Fig. 5).[21,22] It was reported[24] that for the formation of 3D porous structures from 2D nanosheets, surfactants are indispensable as they can cap the crystal surface selectively and the face with high density of surface atoms is blocked by the adsorption of surfactants during crystal growth. However, in our present study surfactants or other reagents are not used and the 3D microflowers were observed with superior control over shape and size. Scherrer analysis for the average crystal size of the final calcination product at 600 °C, gave size range of 20–23 nm.

3.5.   Surface area analysis

Fig. 6 shows the typical sorption isotherms of In_2O_3 microflowers. The prepared In_2O_3 microflowers exhibited a hysteresis
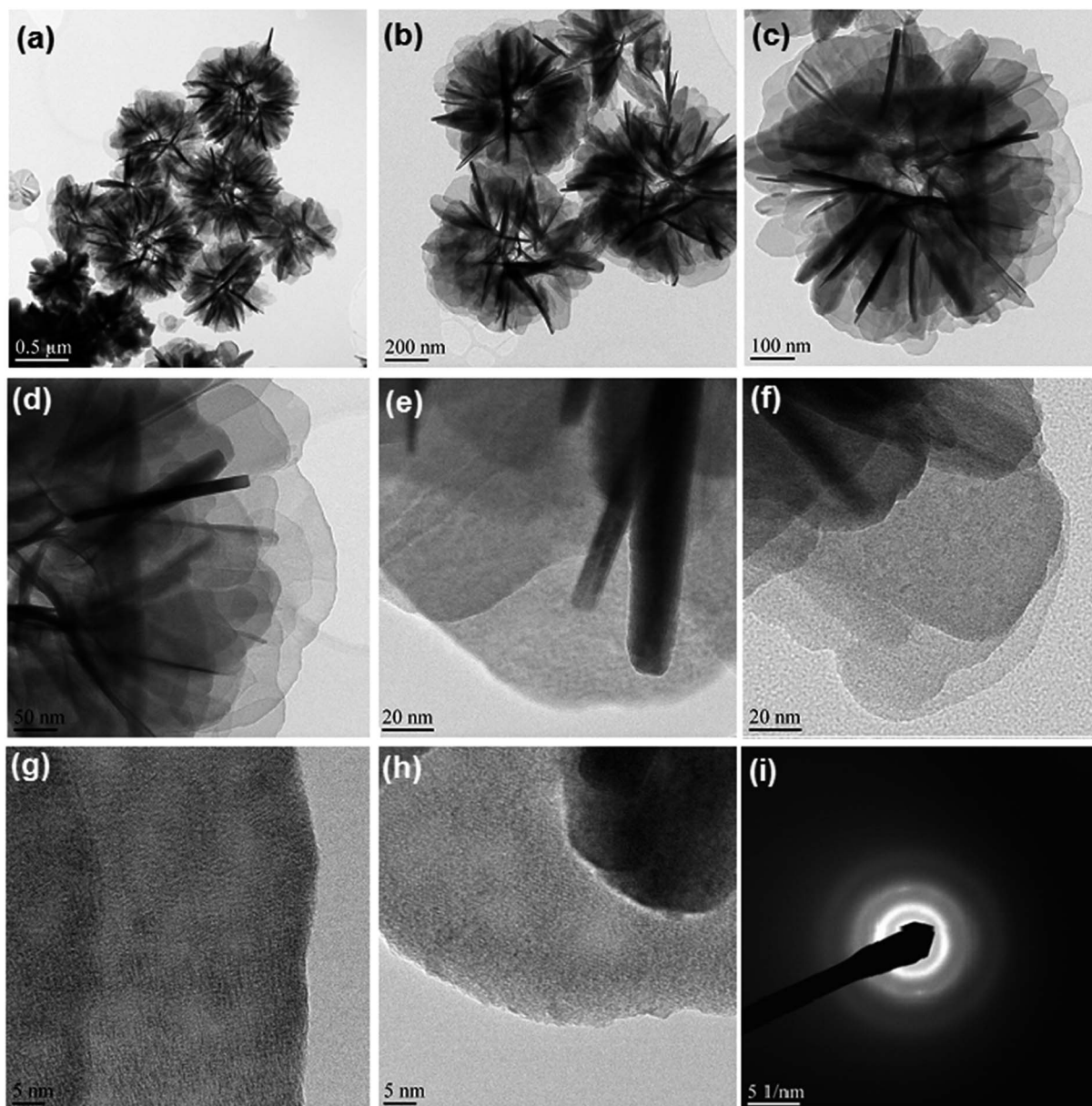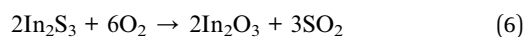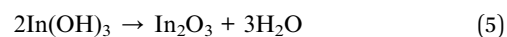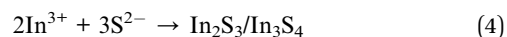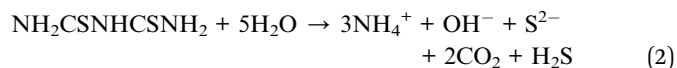
Fig. 3 TEM images of hydrothermal product; (a–c) overall images of microflowers; (d–f) images of thin petals of microflowers; (g and h) images showing sharp edges of petals (i) SAED pattern of hydrothermal product.

loop in a high relative pressure range of 0.77 to 0.98, which is characteristic of type IV isotherm according to IUPAC classification and evidences the presence of mesopores. The observed BET surface area is 70.28 $m^2\ g^{-1}$ for In_2O_3 microflowers which is higher compared to the reported In_2O_3 porous materials.[7,9] The total pore volume is 0.154 $cm^3\ g^{-1}$ and the average pore diameter is 1.518 nm. The observed results exemplify the mesoporous nature of In_2O_3 microflowers. Since the surface area is very high it may have potential application as a catalyst or in gas storage.

3.6. Hydrothermal reactions, growth mechanism and calcination reactions

In the described synthetic process we have used dithiobiuret as a sulfur source which, together with indium salt ($In(NO_3)_3$), was expected to give indium sulfide during hydrothermal process. To our surprise we observed the formation of $In(OH)_3$ as a major hydrothermal product along with the formation of In_2S_3 and In_3S_4 as minor products. The whole hydrothermal and calcination process can be explained by the following eqn (2)–(6).

$$NH_2CSNHCSNH_2 + 5H_2O \rightarrow 3NH_4^+ + OH^- + S^{2-} + 2CO_2 + H_2S \quad (2)$$

$$In^{3+} + 3OH^- \rightarrow In(OH)_3 \quad (3)$$

$$2In^{3+} + 3S^{2-} \rightarrow In_2S_3/In_3S_4 \quad (4)$$

$$2In(OH)_3 \rightarrow In_2O_3 + 3H_2O \quad (5)$$

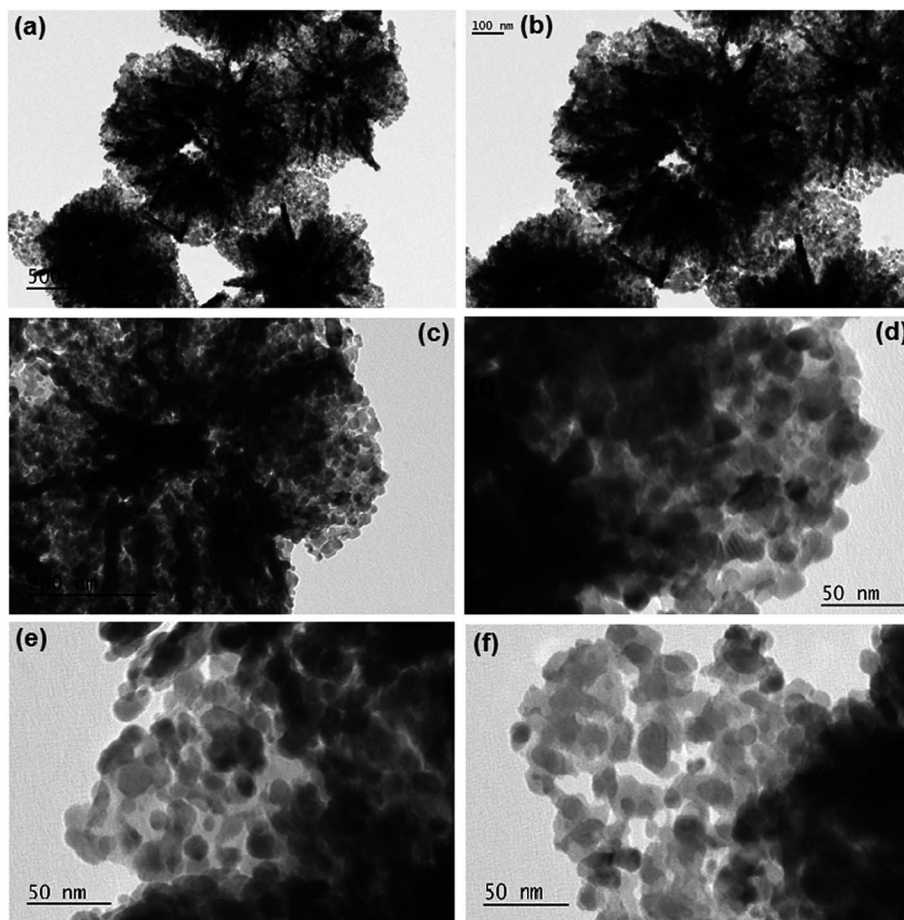$$2In_2S_3 + 6O_2 \rightarrow 2In_2O_3 + 3SO_2 \quad (6)$$

Fig. 4 TEM images of In_2O_3 microflowers; (a–c) low magnification TEM images; (d–f) high magnification TEM images.

In this process dithiobiuret decomposes slowly leading to a low degree of supersaturation in solution and resulting in the nucleation between S^{2-} and In^{3+} ions at the initial period of the hydrothermal treatment as shown in eqn (2) and (4). Although the dithiobiuret releases S^{2-} ions thus generating In_2S_3/In_3S_4,

the formation of $In(OH)_3$ under hydrothermal conditions (eqn (3)) is prevalent over indium sulfide(s) formation due to the presence of excess OH^-. The formation of $In(OH)_3$ has not been previously reported in the synthesis of In_2S_3 under hydrothermal conditions with various other sulfur sources such as thioacetamide, L-cysteine, thiourea, sodium thiosulfate, elemental sulfur and dithiocarbamate.[21–33] On the other hand,
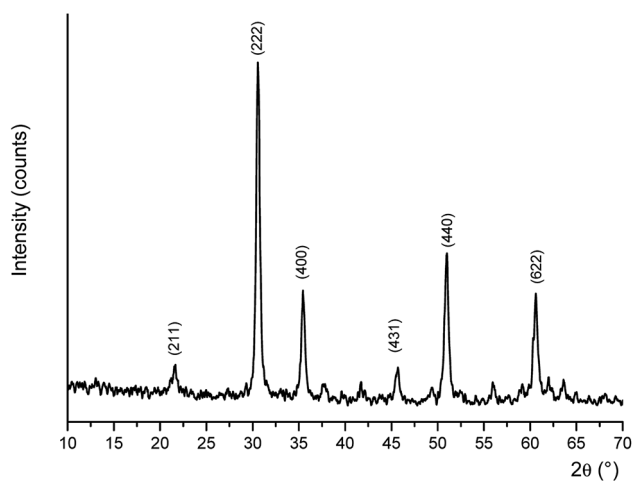

Fig. 5 X-ray powder diffraction pattern of the product calcinated at 600 °C for 2 h. Characteristic peak positions of In_2O_3 are indicated by their Miller indices.

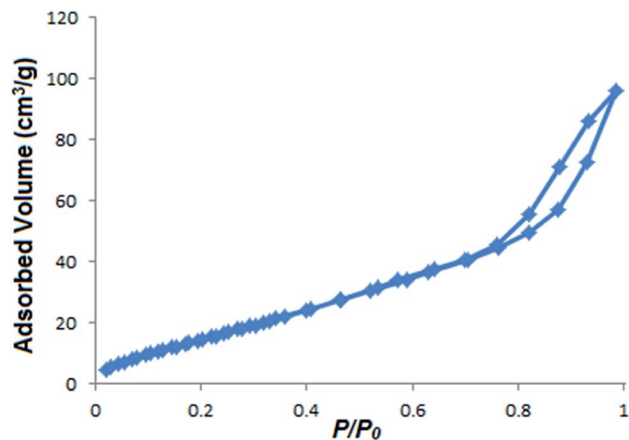**Fig. 6** Nitrogen adsorption–desorption isotherm of In_2O_3 micro flowers.

the formation of $In(OH)_3$ has been shown to occur in the absence of sulfur sources *via* direct hydrolysis of simple indium salts, such as $In(NO_3)_3$, under hydrothermal conditions.[13] Hence, in our system, the degradation of dithiobiuret into OH^- and S^{2-} ions results into a competition between the formation of $In(OH)_3$ and In_2S_3/In_3S_4 from which the predominant species is probably $In(OH)_3$ since its formation is favored under hydrothermal conditions. In addition to acting as a sulfide and hydroxide source, dithiobiuret is as a shape controlling agent and an organic base and has a clear impact on the formation of the observed uniform and visually appealing morphology of microflowers with sharp edges. Microflowers are formed during the hydrothermal process from nanoscopic petals (nanoflakes) in the absence of surfactants or templates. The process could be explained in terms of Ostwald ripening mechanism according to which the nanoflakes are formed at the expense of the smaller nuclei that are formed initially (Fig. S5†). In nano particles different crystal planes have different surface energies, and of those the planes having the higher surface energies are preferred by crystal growth mechanism defined as Oswald ripening (wherein larger particles tend to grow further by expense of smaller particles).[39] For the minimization of surface energy, flakes aggregate to form a spherical structure during the surface kinetics process, finally resulting in the formation of hierarchical microflowers. The lateral growth through the spherical diffusion model was proposed already[23] for the formation of flake-like morphologies from smaller nuclei.[36] Subsequently, the flakes act as building blocks and point towards the common center thereby creating the obtained flower-like morphology. The lateral growth through the mass transfer process at the hydrothermal conditions has been discussed already.[39]

During the calcination process, the precursors were converted into In_2O_3 as shown in eqn (5) and (6). The exhaustion of sulfur atoms, which has been shown to occur in oxidation of In_2S_3 to In_2O_3,[21] was ruled out in our case as we have not observed any formation of elemental sulfur during the calcination process. In such case, SO_2 would have been liberated and the evaporation of SO_2 molecules would then result in the destruction of flake-like structure and to the formation of small indium oxide nanoparticles. However, the absence of such particles was unequivocally proved by SEM and TEM measurements. The conversion of the hydrothermal product to In_2O_3 was partial after 2 h at 400 °C (Fig. S4†). The precursors are completely converted into In_2O_3 after 6 h at 600 °C which was evidenced by PXRD wherein the obtained pattern lacks diffraction peaks originating from other crystalline phases (Fig. 5). It is noteworthy that $In(OH)_3 \rightarrow In_2O_3$ conversion is straightforward and other products like oxyhydroxides (InOOH) are not formed during the calcination.

3.7. Effect of reaction parameters and additives

It was clear that the increase in reaction time resulted in slight increase in the dimensions of microflowers and also thickening of petals.[28] This could be due to the deposition of smaller nuclei to the larger crystals formed already. Similarly, changing the reactants ratio does not have a meaningful influence on the morphology of microflowers. Whereas, extending the calcination to 10 h results in the breaking of microflower structure by creating holes with the size range of 100 to 200 nm [Fig. 7a–c]. Interestingly, the addition of ethylenediamine seems to have a spectacular effect on the nanoparticle morphology as spherical and oval shapes are formed [Fig. 7d] whereas the
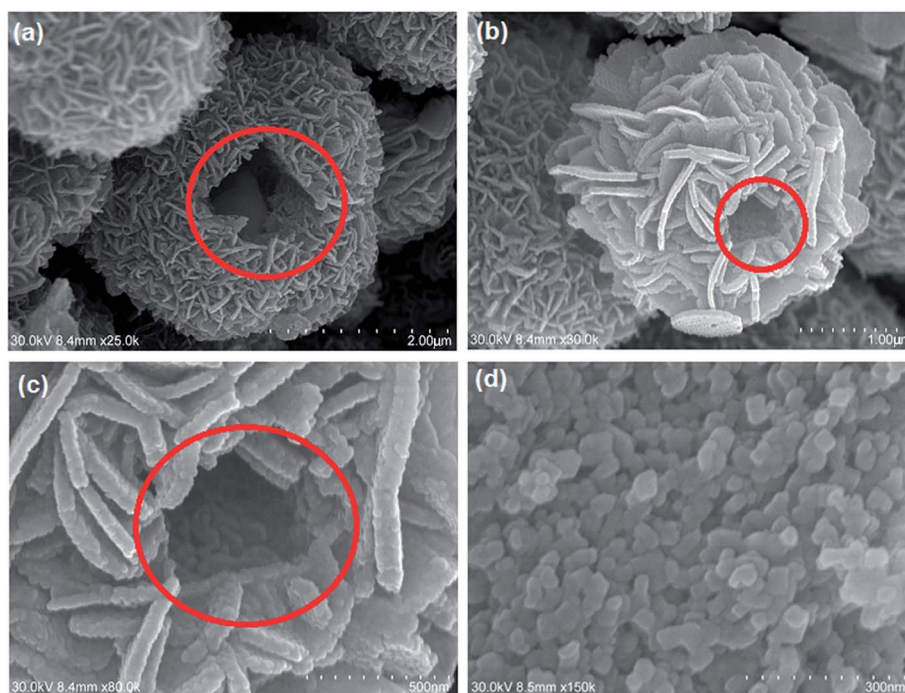

Fig. 7 SEM images of (a–c) broken In_2O_3 microstructures; (d) In_2O_3 nanoparticles formed with the addition of EDA during hydrothermal process.
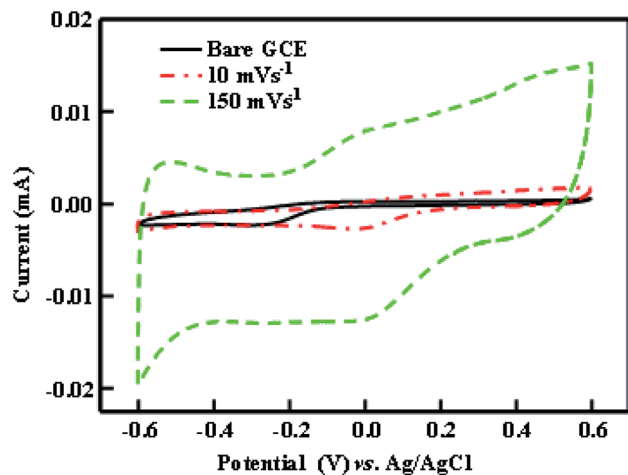
Fig. 8 Cyclic voltammograms (CVs) of bare GCE and In$_2$O$_3$/GCE electrodes in 1 M Na$_2$SO$_4$ electrolyte.

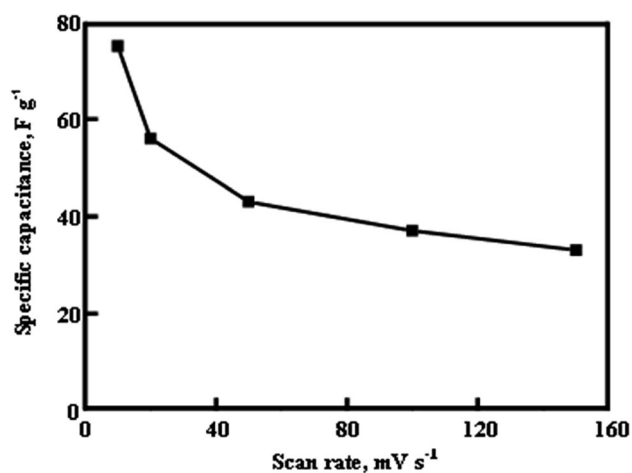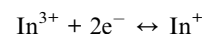

Fig. 9 Specific capacitance of In$_2$O$_3$/GCE electrodes against the scan rate.

microflower morphology was not anymore observed. We are currently exploring the effects of different additives on morphology and report these results at a later time.

3.8. Electrochemical studies

Fig. 8 shows the typical cyclic voltammogram (at various scan rates) of In$_2$O$_3$ on glassy carbon electrode (GCE) in 1 M Na$_2$SO$_4$ between −0.6 to 0.6 V vs. Ag/AgCl. In general, the area under the CV curve represents the amount of charge stored in the electrode material. In the CV curve, two quasi reversible redox peaks are observed which illustrate the sequential transitions of In^{3+} to In$^+$. The main pseudocapacitance behaviour of the sample can be attributed to the quasi-reversible redox transition of In^{3+} to In$^+$ and *vice versa*.[40] The capacitive behaviour of In$_2$O$_3$ is clearly seen from the figure with near rectangular shaped voltammograms and larger CV currents. Nevertheless, In$_2$O$_3$ has various reduction potential ranges from −0.14 to −1.034 (SHE), the one observed at −0.52 V against Ag/AgCl indicates that the synthesized In$_2$O$_3$ is in In^{3+} which is reduced to In$^+$ under the given potential. The possible redox reaction can be written as

$$In^{3+} + 2e^- \leftrightarrow In^+$$

The specific capacitance values as a function of scan rate of CV are shown in Fig. 9. The SC value of 75 F g^{-1} and 37 F g^{-1} has been obtained at the scan rate of 10 mV s^{-1} and 100 mV s^{-1} respectively. The specific capacitance of the electrode is decreased with increase of scan rate. The reason for the variation of specific capacitance with scan rate can be explained with the following points; (i) at high scan rate, the ions from electrolyte have less accessible time to diffuse into the electrode material resulting in lower specific capacitance. Hence, only limited amount of charge is stored (surface) which leads to decrease of specific capacitance, (ii) at low scan rate, the ions from electrolyte have the ability to access both inner and outer surface of the electrode material which leads to higher specific capacitance. Comparison of specific capacitance values for In$_2$O$_3$ materials reported in literature and from this work is shown in Table 1.

The reduced specific capacitance for the synthesized In$_2$O$_3$ micro flower (in this work) may be due to the mesoporous nature of 3D sheets of In$_2$O$_3$. The mesoporous material may hold the ions for a longer time and hence the amount of charge on the surface gets decreased and also the specific capacitance.

Table 1 Comparison of specific capacitance values of In$_2$O$_3$ materials

| In$_2$O$_3$ materials	Specific capacitance
Porous indium oxide hollow spheres (PIOHS)[41]	320 F g^{-1} and 185 F g^{-1} @ 1 A g^{-1}
In$_2$O$_3$ nanoparticles/CNT[42]	64 F g^{-1}
In$_2$O$_3$-impregnated mesoporous carbon[42]	275 F g^{-1}
Nano rod In$_2$O$_3$ (ref. 43)	104.9 F g^{-1} @ 8 A g^{-1}
Nanostructured indium oxide[44]	190 F g^{-1} @ 10 mV s^{-1}
	80 F g^{-1} @ 1000 mV s^{-1}
In$_2$O$_3$ nanostructures[45]	
(a) Nanotowers	10.1 mF cm^{-2}
(b) Nanobouquets	12.5 mF cm^{-2}
(c) Nanocones	4.9 mF cm^{-2}
(d) Nanowires	16.6 mF cm^{-2}
In this work	75 F g^{-1} @ 10 mV s^{-1}
	37 F g^{-1} @ 100 mV s^{-1}
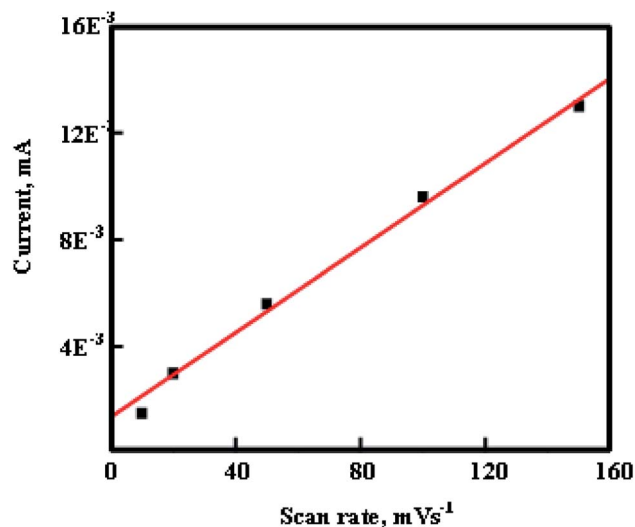
Fig. 10 CV current of In_2O_3/GCE electrodes against the scan rate.

Fig. 10 clearly indicates that the CV currents increase linearly with an increase in scan rate which shows the high power property of In_2O_3. At a high scan rate, a large value of specific capacitance indicates that In_2O_3 can be a promising material for redox supercapacitors.

4. Conclusions

Porous In_2O_3 microstructures were prepared from indium nitrate and dithiobiuret by hydrothermal and subsequent calcination method. The hydrothermal reaction products (which is a mixture of $In_2S_3/In(OH)_3$) show 3D hierarchical architectures and were obtained by the self-assembly process with the involvement of Ostwald ripening mechanism. The microflowers are made of small 2D nanosheets with thickness of 20–30 nm. These thin nanosheets, analogous to petals of flowers, and are aligned to the spherical surface of the microflowers, pointing toward a common center. Calcination resulted in porous In_2O_3 microflowers which retained their morphology. The mechanism of hydrothermal and calcination reactions were discussed in detail. Effect of reaction parameters and additives were explored. Average crystal size of In_2O_3 nanoparticles was estimated to be about 23 nm. Cyclic voltammetric studies reveal the quasi-reversible redox transition of In^{3+} to In^+ and *vice versa*. Specific capacitance values as a function of scan rate of CV were calculated. Surface area analysis reveals the mesoporous nature of the synthesized material (In_2O_3). With the decent surface area the synthesized In_2O_3 hierarchical microarchitechtures composed of nanosheets may have potential application as a catalyst or in gas storage.

Conflicts of interest

There are no conflicts to declare.

References

1 W. Y. Chung, G. Sakai, K. Shimanoe, N. Miura, D. D. Lee and N. Yamazoe, *Sens. Actuators, B*, 1998, **46**, 139–145.

2 H. Cao, X. Qiu, Y. Liang, Q. Zhu and M. Zhao, *Appl. Phys. Lett.*, 2003, **83**, 761–763.

3 M. Liess, *Thin Solid Films*, 2002, **410**, 183–187.

4 J. Tamaki, C. Naruo, Y. Yamamoto and M. Matsuoka, *Sens. Actuators, B*, 2002, **83**, 190–194.

5 E. Gagaoudakis, M. Bender, E. Douloufakis, N. Kataarakis, N. Natsakou, V. Cimalla and G. Kiriakids, *Sens. Actuators, B*, 2001, **80**, 155–161.

6 S. Parthiban, K. Ramamurthi, E. Elangovan, R. Martins and E. Fortunato, *Appl. Phys. Lett.*, 2009, **94**, 212101–212103.

7 Z. He, Z. Chen, Y. Li, Q. Zhang and H. Wang, *CrystEngComm*, 2011, **13**, 2557–2565.

8 H. Y. Lai, T. H. Chen and C. H. Chen, *CrystEngComm*, 2012, **14**, 5589–5595.

9 J. Zai, J. Zhu, R. Qi and X. Qian, *J. Mater. Chem. A*, 2013, **1**, 735–745.

10 Z. Li, Y. Li, Y. Luan, J. Li and A. Song, *CrystEngComm*, 2013, **15**, 1706–1714.

11 D. Han, P. Song, H. Zhang, H. Yan, Q. Xu, Z. Yang and Q. Wang, *RSC Adv.*, 2014, **4**, 50241–50248.

12 S. Guo, X. Zhang, Z. Hao, Z. Gao, G. Li and L. Liu, *RSC Adv.*, 2014, **4**, 31353–31361.

13 J. Yang, C. Lin, Z. Wang and J. Lin, *Inorg. Chem.*, 2006, **45**, 8973–8979.

14 Z. Zhuang, Q. Peng, J. Liu, X. Wang and Y. Li, *Inorg. Chem.*, 2007, **46**, 5179–5187.

15 X. Liu, L. Zhou, R. Yi, N. Zhang, R. Shi, G. Gao and G. Qiu, *J. Phys. Chem. C*, 2008, **112**, 18426–18430.

16 D. V. Shinde, D. Y. Ahn, V. V. Jadhav, D. Y. Lee, N. K. Shrestha, J. K. Lee, H. Y. Lee, R. S. Mane and S. H. Han, *J. Mater. Chem. A*, 2014, **2**, 5490–5498.

17 Q. Wu, J. Chen, F. Zhang, P. Xiao, Y. Lu, X. Wang and Z. Hu, *CrystEngComm*, 2012, **14**, 3397–3403.

18 C. Wang, D. Chen and X. Jiao, *J. Phys. Chem. C*, 2009, **113**, 7714–7718.

19 H. Yang, L. Liu, H. Liang, J. Wei and Y. Yang, *CrystEngComm*, 2011, **13**, 5011–5016.

20 S. Wang, P. Wang, Z. Li, C. Xiao, B. Xiao, R. Zhao, T. Yang and M. Zhang, *New J. Chem.*, 2014, **38**, 4879–4884.

21 A. Datta, S. K. Panda, D. Ganguli, P. Mishra and S. Chaudhuri, *Cryst. Growth Des.*, 2007, **7**, 163–169.

22 P. Zhao, T. Huang and K. Huang, *J. Phys. Chem. C*, 2007, **111**, 12890–12897.

23 J. Liu, T. Luo, F. Meng, K. Qian, Y. Wan and J. Liu, *J. Phys. Chem. C*, 2010, **114**, 4887–4894.

24 L. Liu, H. Liu, H. Kou, Y. Wang, Z. Zhou, M. Ren, M. Ge and X. He, *Cryst. Growth Des.*, 2009, **9**, 113–117.

25 S. Avivi, O. Palchik, V. Palchik, M. A. Slifkin, A. M. Weiss and A. Gedanken, *Chem. Mater.*, 2001, **13**, 2195–2200.

26 K. Xue, D. Chen and X. Jiao, *Inorg. Chem.*, 2010, **49**, 1191–1197.

27 L. Y. Chen, Z. D. Zhang and W. Z. Wang, *J. Phys. Chem. C*, 2008, **112**, 4117–4123.

28 Y. Xiong, Y. Xie, G. Du and X. Tian, *J. Mater. Chem.*, 2002, **12**, 98–102.

29 M. Afzaal, M. A. Malik and P. O'Brien, *Chem. Commun.*, 2004, 334–335.

30 J. Tabernor, P. Christian and P. O'Brien, *J. Mater. Chem.*, 2006, **16**, 2082–2087.

31 B. G. Kumar and K. Muralidharan, *J. Mater. Chem.*, 2011, **21**, 11271–11275.

32 G. Liu, X. Jiao, Z. Qin and D. Chen, *CrystEngComm*, 2011, **13**, 182–187.

33 A. K. Nayak, S. Lee, Y. Sohn and D. Pradhan, *CrystEngComm*, 2014, **16**, 8064–8072.

34 X. Ren, H. Fan, J. Ma, C. Wang, M. Zhang and N. Zhao, *Appl. Surf. Sci.*, 2018, **441**, 194–203.

35 M. Zhang, H. Fan, N. Zhao, H. Peng, X. Ren, W. Wang, H. Li, G. Chen, Y. Zhu, X. Jiang and P. Wu, *Chem. Eng. J.*, 2018, **347**, 291–300.

36 J. Ma, H. Fan, H. Tian, X. Ren, C. Wang, S. Gao and W. Wang, *Sens. Actuators, B*, 2018, **262**, 17–25.

37 P. Li, H. Fan, Y. Cai, M. Xu, C. Long, M. Li, S. Lei and X. Zou, *RSC Adv.*, 2014, **4**, 15161–15170.

38 B. Arul Prakasam, M. Lahtinen, M. Muruganandham and M. Sillanpää, *Mater. Lett.*, 2015, **158**, 370–372.

39 W. Shi, S. Song and H. Zhang, *Chem. Soc. Rev.*, 2013, **42**, 5714–5743.

40 N. R. Armstrong, A. W. C. Lin, M. Fujihira and T. Kuwana, *Anal. Chem.*, 1976, **48**, 741–750.

41 R. Kumar, A. Agrawal, T. Bhuvana and A. Sharma, *Electrochim. Acta*, 2018, **270**, 87–95.

42 B. P. Bastakoti, H. Oveisi, C. Hu, C. Kevin, W. Wu, N. Suzuki, K. Takai, Y. Kamachi, M. Imura and Y. Yamauchi, *Eur. J. Inorg. Chem.*, 2013, 1109–1112.

43 J. Chang, W. Lee, S. Rajaram, S. Mane, B. Won Cho and S.-H. Han, *Electrochem. Solid-State Lett.*, 2008, **11**(1), A9–A11.

44 K. R. Prasad, K. Koga and N. Miura, *Chem. Mater.*, 2004, **16**, 1845–1847.

45 F. N. Tuzluca, Y. O. Yesilbag and M. Ertugrul, *Appl. Surf. Sci.*, 2018, **427**, 956–964.